HAL
open science

Circuit quantum electrodynamics of granular aluminum resonators

N. Maleeva, L. Grünhaupt, T. Klein, F. Levy-Bertrand, O. Dupré, M. Calvo, F. Valenti, P. Winkel, F. Friedrich, W. Wernsdorfer, et al.

To cite this version:

N. Maleeva, L. Grünhaupt, T. Klein, F. Levy-Bertrand, O. Dupré, et al.. Circuit quantum electrodynamics of granular aluminum resonators. Nature Communications, 2018, 9, pp.3889. 10.1038/s41467-018-06386-9 . hal-01886934

HAL Id: hal-01886934

https://hal.science/hal-01886934v1

Submitted on 15 Dec 2023

HAL is a multi-disciplinary open access archive for the deposit and dissemination of scientific research documents, whether they are published or not. The documents may come from teaching and research institutions in France or abroad, or from public or private research centers.

L'archive ouverte pluridisciplinaire **HAL**, est destinée au dépôt et à la diffusion de documents scientifiques de niveau recherche, publiés ou non, émanant des établissements d'enseignement et de recherche français ou étrangers, des laboratoires publics ou privés.

nature COMMUNICATIONS

ARTICLE

DOI: 10.1038/s41467-018-06386-9 OPEN

Circuit quantum electrodynamics of granular aluminum resonators

N. Maleeva[1], L. Grünhaupt[1], T. Klein[2,3], F. Levy-Bertrand[2,3], O. Dupre[2,3], M. Calvo[2,3], F. Valenti[1], P. Winkel[1], F. Friedrich[1], W. Wernsdorfer[1,3,4], A.V. Ustinov[1,5], H. Rotzinger[1], A. Monfardini[2,3], M.V. Fistul[5,6] & I.M. Pop[1,7]

Granular aluminum (grAl) is a promising high kinetic inductance material for detectors, amplifiers, and qubits. Here we model the grAl structure, consisting of pure aluminum grains separated by thin aluminum oxide barriers, as a network of Josephson junctions, and we calculate the dispersion relation and nonlinearity (self-Kerr and cross-Kerr coefficients). To experimentally study the electrodynamics of grAl thin films, we measure microwave resonators with open-boundary conditions and test the theoretical predictions in two limits. For low frequencies, we use standard microwave reflection measurements in a low-loss environment. The measured low-frequency modes are in agreement with our dispersion relation model, and we observe self-Kerr coefficients within an order of magnitude from our calculation starting from the grAl microstructure. Using a high-frequency setup, we measure the plasma frequency of the film around 70 GHz, in agreement with the analytical prediction.

[1] Physikalisches Institut, Karlsruhe Institute of Technology, Wolfgang-Gaede-Str. 1, 76131 Karlsruhe, Germany. [2] Universite Grenoble Alpes, Institut NEEL, 25 rue des Martyrs BP 166, F-3800 Grenoble, France. [3] CNRS, Institut NEEL, 25 rue des Martyrs BP 166, F-3800 Grenoble, France. [4] Institute of Nanotechnology, Karlsruhe Institute of Technology, 76344 Eggenstein Leopoldshafen, Germany. [5] Russian Quantum Center, National University of Science and Technology MISIS, Leninskiy prsp., 4, 119049 Moscow, Russia. [6] Center for Theoretical Physics of Complex Systems, Institute for Basic Science, Expo-ro 55, Yuseong-gu 34051 Daejeon, Republic of Korea. [7] Institute of Nanotechnology, Karlsruhe Institute of Technology, Hermann-von-Helmholtz-Platz 1, 76344 Eggenstein Leopoldshafen, Germany. Correspondence and requests for materials should be addressed to I.M.P. (email: ioan.pop@kit.edu)

The introduction of crystalline defects or dopants can give rise to so-called dirty superconductors[1], characterized by reduced coherence length and quasiparticle mean free path. In particular, granular superconductors[2] such as grAl[3,4], consisting of remarkably uniform grains connected by Josephson contacts[5] have attracted interest since the 60s, thanks to their rich phase diagram[6,7] and practical advantages, like increased critical temperature[4,8], critical field[9,10], and kinetic inductance[11]. Here we report the measurement and modeling of circuit quantum electrodynamics[12] properties of grAl microwave resonators in a wide frequency range, up to the spectral superconducting gap. Interestingly, we observe self-Kerr coefficients ranging from 10^{-2} Hz to 10^5 Hz, within an order of magnitude from analytic calculations based on grAl microstructure. This amenable nonlinearity, combined with the relatively high-quality factors in the 10^5 range, open new avenues for applications in quantum information processing[13] and kinetic inductance detectors[14].

Increasing the level of disorder in a superconducting material usually decreases the superfluid density and can induce a superconducting to insulating transition. Superconductors with low superconducting carrier density can exhibit rich physical properties, arising from a variety of phenomena such as quantum phase transitions[15] and localization[2]. Granular aluminum is a typical example preferred by experimentalists, thanks to its relatively straightforward fabrication by aluminum evaporation in an oxygen atmosphere[3], which can tune the film resistivity ρ over five orders of magnitude. The phase diagram of grAl thin films, with an initial increase of the critical temperature versus resistivity[16], followed by a decrease and transition to an insulating state, has been extensively studied over the last 50 years, with notable recent developments in both theory[17] and experiment[18,19]. These studies, mostly performed by direct current measurements, or broadband THz spectroscopy, offer a solid basis to start addressing the electrodynamics of grAl in the quantum regime, defined as the limit of single-photon excitations.

In the context of emerging quantum information platforms based on aluminum[13], grAl provides precious ingredients such as low-loss and high-impedance environments, tolerance to high magnetic fields, or a robust source of nonlinearity. The prospect of implementing ultra-high impedance environments, at the level of the impedance quantum $R_Q = h/(2e)^2 \simeq 6.5\,\mathrm{k}\Omega$, for the design of qubits[20–22] and parametric amplifiers[23] or for the engineering of quantum states of light[24] is very appealing. However, the electromagnetic properties of granular superconductors in the quantum regime are currently virtually unexplored.

Here we present a theoretical model and the corresponding experimental investigation of the dispersion relation and nonlinear Kerr coefficients for grAl resonators in the microwave regime. We will use the formalism of circuit quantum electrodynamics[12] (cQED) and show that in a first-order approximation, the Hamiltonian of grAl, taking into account the interaction between the resonant modes, can be written in the familiar quantum optics form[25]

$$\frac{H}{\hbar} = \sum_{n=1} \left(\omega_n + K_{nn} a_n^\dagger a_n\right) a_n^\dagger a_n + \sum_{n,m=1;\, n\neq m} \frac{K_{nm}}{2} a_n^\dagger a_n a_m^\dagger a_m. \tag{1}$$

The frequencies ω_n form the dispersion relation, the self-Kerr coefficients K_{nn} quantify the frequency shift of mode n for each added photon, and the cross-Kerr coefficients K_{nm}, quantify the frequency shift of mode n for an added photon in mode m. The operators a_n and $a_n^\dagger$ are bosonic lowering and raising operators, and $a_n^\dagger a_n = N$ gives the photon number.

Results

Electrodynamic model. The microstructure of grAl consists of pure aluminum grains, with the average diameter a, separated by thin aluminum oxide barriers, as schematically illustrated in Fig. 1a. For films fabricated at room temperature with $\rho > 10\,\mu\Omega$ cm, the grain size is homogeneous and independent of resistivity, $a = 3 \pm 1$ nm[4]. We use grAl films with a resistivity between 40 $\mu\Omega$ cm and 4000 $\mu\Omega$ cm, below the superconducting to insulating transition at $\rho \simeq 10^4\,\mu\Omega$ cm[7], and for which the kinetic inductance dominates over the geometric inductance[11]. We model this medium as a network of effective Josephson junctions (JJ), which provides a handle to calculate its dispersion relation[26] and the Kerr coefficients[27,28].

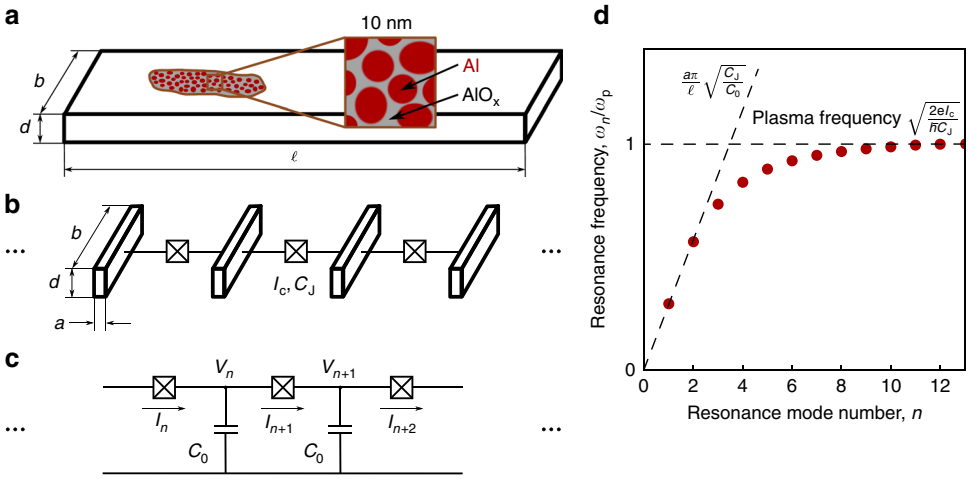

Fig. 1 Schematic representation of a grAl stripline resonator with open-boundary conditions. **a** The length of the stripline, ℓ, is in the range of mm, its width, b, is in the range of a few μm, and the thickness, d, is between 20 and 30 nm. Al grains (sketched in bordeaux color in the inset) have a diameter $a = 3 \pm 1$ nm[4]. They are separated by aluminum oxide barriers (shown in gray), forming a 3D network of superconducting islands connected by Josephson contacts. **b** For the lowest-frequency standing-current modes along the stripline, the resonator can be modeled as a 1D array of effective Josephson junctions with critical current I_c and junction capacitance C_J, corresponding to the summed critical currents and capacitances of the grains in a stripline section of length a. **c** The resulting circuit diagram consists of identical cells, each containing an effective JJ and the self capacitance C_0 of the superconducting island. **d** Typical dispersion relation of a 1D JJ array, following Eq. (3). The spectrum saturates at the effective plasma frequency $\omega_p = \sqrt{2eI_c/\hbar C_J}$. The slope in the linear part of the dispersion relation is defined by the ratio $\frac{a\pi}{\ell}\sqrt{C_J/C_0}$

For elongated structures, such as stripline resonators (Fig. 1a), the calculation of the low-frequency dispersion relation and nonlinearity can be performed in the limit of one-dimensional (1D) current distributions along the stripline (see Supplementary Discussion), resulting in an effective JJ chain model (see Fig. 1b). The current is homogeneously distributed through the sample cross-section due to the fact that the thickness $d \simeq 20$ nm is much smaller than the magnetic field penetration depth, $\lambda_L > 0.4$ µm, depending on the film resistivity ρ, and the width b is smaller than the screening distance, $\lambda_\perp = \lambda_L^2/d > 8$ µm[3]. The equivalent electrical schematics is shown in Fig. 1c, where each superconducting section of length a with self capacitance C_0 is connected by effective JJs with critical current I_c and capacitance C_J.

The classical equation of motion for the phase difference φ_n across the nth JJ is

$$\begin{aligned} &2I_c \sin(\varphi_{n+1}) - I_c \sin(\varphi_{n+2}) - I_c \sin(\varphi_n) + \\ &+ \tfrac{\hbar C_J}{2e} \tfrac{d^2}{dt^2} (2\varphi_{n+1} - \varphi_{n+2} - \varphi_n) + \\ &+ \delta_{m,n} I_{\mathrm{ext}} \cos(\omega t) = \tfrac{\hbar C_0}{2e} \tfrac{d^2 \varphi_n}{dt^2}. \end{aligned} \tag{2}$$

The resonator drive is introduced as an external current applied to the mth cell, $\delta_{m,n} I_{\mathrm{ext}} \cos(\omega t)$, where $\delta_{m,n}$ is the Kronecker delta. In order to derive the eigenfrequencies, we use first-order Taylor expansion for the Josephson currents (see Supplementary Discussion). Thus we obtain the dispersion relation:

$$\omega_n = \frac{na\pi}{l} \sqrt{\frac{2eI_c}{\hbar\left(C_0 + \frac{n^2\pi^2a^2}{l^2} C_J\right)}}, \tag{3}$$

sketched in Fig. 1d, which is approximately linear for the lowest modes, and it saturates at the effective plasma frequency $\omega_p = \omega_{n=\ell/a} = \sqrt{2eI_c/\hbar C_J}$, as measured on mesoscopic JJ arrays[29]. As we will show in the following, the fundamental frequency $f_1 = \omega_1/2\pi$, designed in the low GHz range, can provide a convenient link through the cross-Kerr effect to the higher modes of the dispersion relation, spanning up to ~100 GHz.

To derive the Kerr coefficients of the fundamental mode in Eq. (1), we solve the equation of motion, expanding the nonlinear terms up to third order. This method is similar to the one recently used to derive the nonlinearity of mesoscopic arrays of JJ[27,30]. By relating the phase response amplitude to the circulating photon number $\bar{N}$ (see Supplementary Discussion), we obtain the self-Kerr and cross-Kerr coefficients for the fundamental mode:

$$K_{1n} = \mathcal{C}\pi e a \frac{\omega_1 \omega_n}{j_c V_{\mathrm{grAl}}}, \text{ with } n \geq 1. \tag{4}$$

Here, e is the electron charge, a is the grain size, $j_c = I_c/bd$ is the critical current density, ω_n are the eigenfrequencies given by Eq. (3), and $V_{\mathrm{grAl}} = bd\ell$ is the volume of grAl threaded by the current, see Fig. 1a. $\mathcal{C}$ is a numerical constant of order one, which for a sinusoidal current distribution is $\mathcal{C} = 3/16$ for $n = 1$ and $\mathcal{C} = 1/4$ for $n > 1$. Using the expression for the single-photon current as a function of frequency and total inductance, $I_{\bar{N}=1}^2 = 2fh/L$ and $L \propto 1/j_c$, Eq. (4), can be rewritten in a qualitatively similar form to the K_{11} coefficient estimated from Mattis–Bardeen theory for dirty superconductors[11,23], $K_{11} \propto (I_{\bar{N}=1}/I_*)^2$. The depairing current I_* is of the same order of magnitude as the critical current of the strip I_c. In contrast, Eq. (4) offers a quantitative model for the nonlinearity of grAl, starting from the film properties. Remarkably, this analytic result agrees within an order of magnitude with the K_{11} coefficients measured on 14 grAl samples, spanning from $K_{11} = 2 \times 10^{-2}$ Hz to $K_{11} = 3 \times 10^4$ Hz.

Furthermore, the cross-Kerr coefficients, K_{1n}, follow the functional dependence of the dispersion relation, ω_n, given by Eq. (3) and reach a maximum at the effective plasma frequency ω_p (see Fig. 1d). Due to the high cross-Kerr interaction and high-mode density around ω_p, we expect a strong response of the fundamental mode for drive frequencies in the vicinity of $\omega_p/2\pi$. As discussed in detail in the next section, for highly resistive samples (grAl#3) with $\rho = 3000$ µΩ cm, for which ω_p is low enough to be in the measurable range, we observe the expected plasma frequency response in the vicinity of 70 GHz.

Measurements. To measure the dispersion relation, microwave losses, and the nonlinearity of grAl structures, we use three types of resonators of various shapes and sizes (see Methods), optimized for two complementary measurement setups (see Fig. 2), covering a broad frequency range up to 200 GHz.

In Fig. 3a, b, we plot a typical amplitude and phase response measured for stripline resonators in the single-photon regime, $\bar{N} \approx 1$, which is relevant for quantum information applications. We extract an internal quality factor $Q_i = 10^5$, comparable to values obtained for JJ array superinductances[29]. We obtain similar results for Q_i measurements on Hilbert-shaped (Fig. 2c) and aluminum-shunted stripline resonators, for tens of resonators, with grAl resistivities up to 4000 µΩ cm, corresponding to ~kΩ characteristic impedance. As discussed in ref.[31], we estimate that Q_i is dominated by non-equilibrium quasiparticle dissipation, which could be suppressed by phonon and quasiparticle traps.

Using a two-tone spectroscopy, similar to a superconducting qubit readout procedure[12], we measure higher modes of the dispersion relation for stripline resonators. Due to the symmetry of the electric field, the next mode, above the fundamental, coupled to the waveguide is the third. For sample grAl#1, we measure $f_1 = 6.287$ GHz and $f_3 = 18.255$ GHz. Notice that the dispersion relation already shows a measurable deviation from linear behavior, $3 \times f_1 - f_3 = 606 \pm 1$ MHz, which, using Eq. (3), allows us to estimate an effective plasma frequency $\omega_p = 68 \pm 0.1$ GHz (see Supplementary Discussion), as shown in Fig. 4a).

Indeed, using a Martin–Puplett Interferometer (MPI) as a broadband illumination source up to 200 GHz and a Hilbert-shaped set of resonators (grAl#3) with similar sheet resistivity as grAl#1 mounted in an optical access cryostat, we observe a shift of the fundamental mode for illumination frequencies in the range 60–80 GHz (red curve in Fig. 4b). This shift is comparable to the pair-breaking response at twice the gap, and significantly above the noise floor. We interpret this response to be the cumulated cross-Kerr shift due to the population of the high-mode density region of the effective plasma frequency (see Fig. 4a).

As expected, for resonators with 50 times higher critical current densities j_c, the effective plasma frequency can no longer be measured (green line in Fig. 4b), as it is above the spectroscopic gap frequency. To confirm the correct calibration of the MPI setup, we measured the response of a standard 25-nm aluminum film using an additional 180-GHz low-pass filter. The MPI measurements (blue line in Fig. 4b) indicate the expected Al spectral gap value of 100 GHz, above which the illumination can break the Cooper pairs, inducing a shift of the fundamental mode and a Q_i decrease[14]. Finally, notice that the spectroscopic gap of samples grAl#2 and grAl#3 increases with resistivity, as expected[7].

To measure the self-Kerr coefficient, K_{11}, we monitor the fundamental frequency as a function of photon population $\bar{N}$ using the low-frequency setup (Fig. 2b). Typical measurement

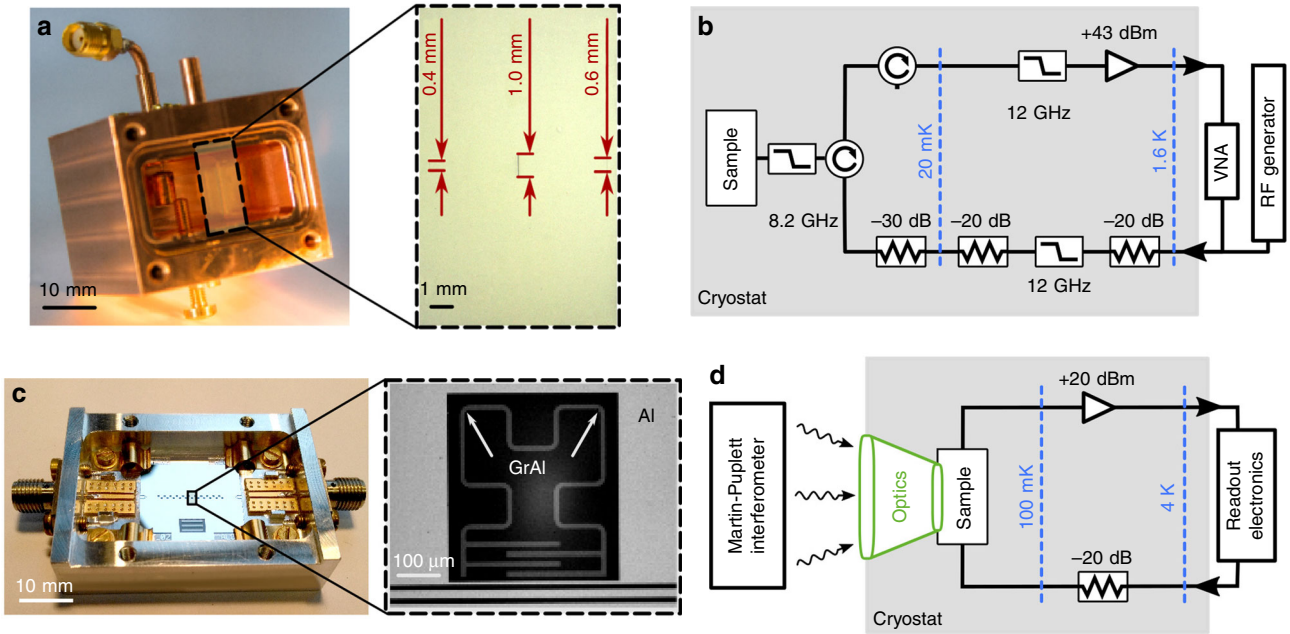

Fig. 2 Two complementary microwave measurement techniques for the study of grAl resonators (grAl#1). Low-frequency setup: **a** Photograph of the Cu waveguide sample holder used to perform reflection measurements on stripline grAl resonators. The inset photograph shows three of the measured resonators, with dimensions $400 \times 5.4\ \mu m^2$, $600 \times 10\ \mu m^2$, and $1000 \times 40\ \mu m^2$. All resonators are 20-nm thick (see Supplementary Discussion). The waveguide is shielded and thermally anchored to the mixing chamber plate of a commercial dilution refrigerator. **b** Schematic of the cryogenic measurement setup. A reflection measurement with a vector network analyzer (VNA) characterizes the resonator response. The total attenuation on the input lines is −70 dB, and both input and output lines are interrupted by commercial and custom-made low-pass filters providing at least −30 dB of filtering above 9 GHz. The output signal is amplified by 40 dB, using a commercial high-electron mobility transistor amplifier. High-frequency setup: **c** Photograph of the Al sample holder and one of the resonators measured using a Martin–Puplett interferometer (MPI). The grAl resonators consist of a second-order Hilbert-shaped fractal inductor and an interdigitated capacitor. Twenty-two resonators are coupled to the common Al feed line, and each resonator is surrounded by an Al ground plane. Notice the different apparent color of the grAl film compared to Al. **d** Schematics of the measurement setup. The resonators are cooled down in a dilution refrigerator with optical access up to 200 GHz, facing the MPI[40]. The optics (shown in green) consist of a lens at room temperature, and two aperture and lens pairs at 4 K and 100 mK, in front of the sample[41]. The grAl resonator response to high-frequency illumination consists in shifting its low-frequency spectrum, which is continuously monitored in a transmission measurement through the common feed line. All samples were fabricated on c-plane, double side polished sapphire substrates, using standard e-beam and optical lithography lift-off techniques

results are shown in Fig. 3c, d in linear and logarithmic scale, respectively. In Fig. 5, we report the measured K_{11} for 14 types of grAl resonators, grouped in three different geometries: KID (in blue), striplines (in green), and Al-shunted striplines (in red); details on the resonators' geometry are given in the Supplementary Discussion. For a direct comparison with Eq. (4) represented by the black line, we plot the measured self-Kerr coefficients versus $f_1^2/j_c V_{grAl}$ using a measured $j_c = 1.1\ mA/\mu m^2$ for $\rho = 1600\ \mu\Omega\ cm$ (see Supplementary Discussion) and scaling it according to $j_c \propto 1/\rho$ for all resistivities[7]. We would like to emphasize that there are no fitting parameters. We estimate the main source of error, responsible for the scatter of the points and for the deviation compared to Eq. (4) to be the photon number calibration. We can only perform this calibration by estimating the total attenuation of the input lines at various frequencies. We estimate this method to be accurate only within a factor of 10. Remarkably, the self-Kerr coefficient of grAl can be tuned over six orders of magnitude by varying the room temperature resistivity $\rho \propto 1/j_c$ and the resonator volume V_{grAl}, without compromising the internal quality factor.

Discussion

According to the strength of the nonlinearity, we can divide the possible grAl applications into three categories. First, for superinductors[29,32–34] and microwave kinetic inductance detectors[14,35,36], the nonlinearity should be as low as possible. The devices plotted in green in Fig. 5 could be used as superinductors with a self-Kerr coefficient of only tens of Hz, which would be at least three orders of magnitude lower than the state-of-the-art[27]. Second, for parametric devices, such as amplifiers[23] or frequency converters[37,38], the self-Kerr coefficient should be in the kHz range, as shown by the devices plotted in red in Fig. 5. Fabricating them using grAl instead of mesoscopic JJ arrays offers the advantages of compactness and single-step fabrication. Finally, in the case of transmon qubits[39], the self-Kerr nonlinearity should be even higher, in the tens of MHz range, which could be achieved by reducing the grAl volume and increasing the resistivity of the film.

In conclusion, granular aluminum is a superconductor with high characteristic impedance, low microwave losses, and amenable nonlinearity, which recommend it as a material of choice for quantum information processing. Using a high-frequency setup, including a Martin–Pupplet interferometer, we observe the effective plasma frequency of highly inductive grAl devices in the range of 70 GHz, which is in agreement with estimates based on a 1D JJ array model and the measured low-frequency spectrum. The measured self-Kerr coefficients agree within an order of magnitude with our analytic model, and they are in the range of applications for parametrically pumped devices, such as quantum amplifiers. Highly inductive grAl films could implement low-loss superinductors for quantum circuits or ultra-sensitive kinetic inductance detectors.

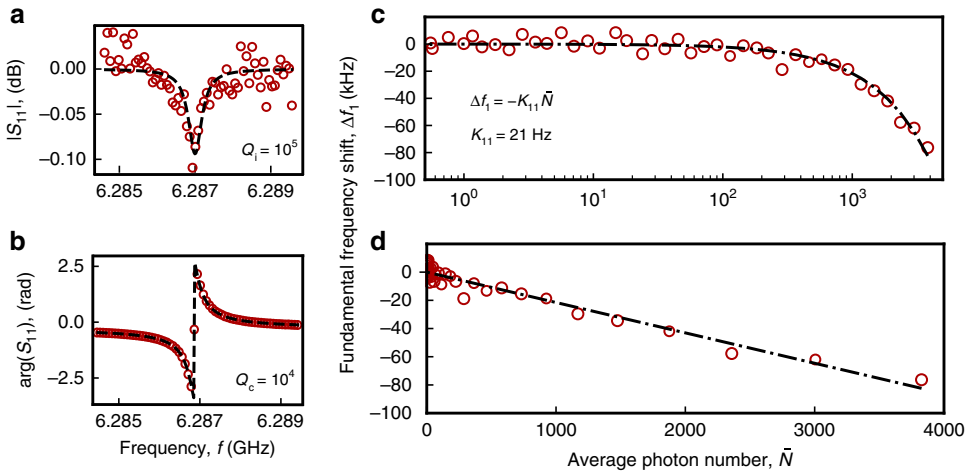

Fig. 3 Measurement of the nonlinearity in grAl resonators. Typical measured amplitude (normalized by the sample holder response) (**a**) and phase (**b**) of the reflection coefficient S_{11} for resonator grAl#1 (see Fig. 2a). We typically observe internal quality factors of the resonators in the range of 10^5. **c**, **d** We plot the measured shift of the first resonant frequency vs. circulating photon number $\bar{N}$ in logarithmic and linear scale, respectively. The corresponding self-Kerr coefficient extracted from the linear fit $K_{11}/2\pi = 21$ Hz. The measured frequency shift remains linear versus photon number for all samples measured below bifurcation, which is consistent with the fact that the estimated circulating current never exceeds ~1% of the critical current

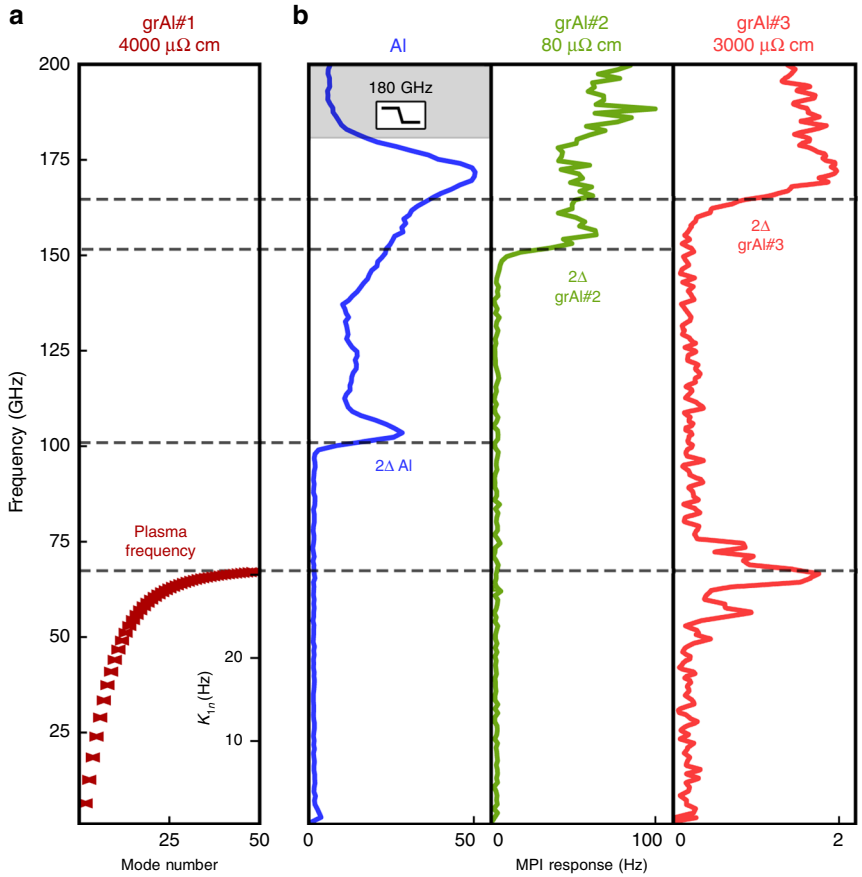

Fig. 4 Measurement of the dispersion relation in grAl resonators. **a** Calculated dispersion relation $f(n)$ for resonator grAl#1 starting from two-tone measurements of the third mode (see text). The spectrum saturates at the effective plasma frequency 68 ± 0.1 GHz. From Eq. (4), the cross-Kerr coefficients follow the dispersion relation, and their values are reported on the right axis. A significant cross-Kerr coupling enables the observation of the high-frequency spectrum up to the effective plasma frequency: photons populating the high end of the spectrum shift the low-lying eigen frequencies, which can be monitored via standard RF transmission measurements (see Fig. 2d). **b** Martin–Puplett Interferometer (MPI) response of Hilbert-shaped resonators made of 25-nm-thick Al, grAl with resistivity 80 μΩ cm (grAl#2), and grAl with resistivity 3000 μΩ cm (grAl#3). The illumination frequencies generated by the MPI range from a few GHz up to 200 GHz, with a resolution of 1 GHz. The different superconducting gaps of the films are evidenced by a strong MPI response due to quasiparticle excitation at 100 GHz for Al, at 150 GHz for grAl#2, and at 165 GHz for grAl#3. For the sample with the highest resistivity and the lowest critical current density, grAl#3, we observe a peak around 65 GHz, in the vicinity of the ω_p predicted from low-frequency measurements on sample grAl#1, with a similarly high resistivity (4000 μΩ cm, see text for details). This MPI response can be seen as the summed dispersive frequency shift due to cross-Kerr interactions K_{1n} between the fundamental mode and all higher populated modes

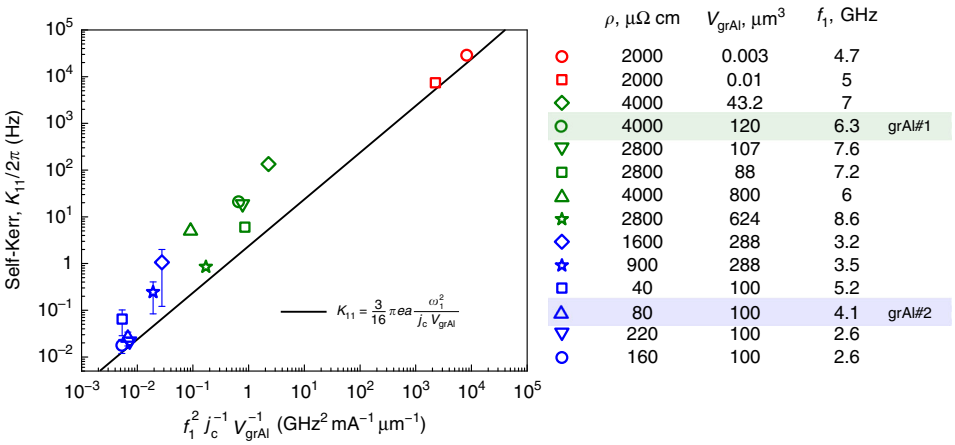

Fig. 5 Measured grAl self-Kerr nonlinearity. The measured self-Kerr coefficients of 14 grAl samples are plotted versus $f_1^2/j_c V_{grAl}$, where $f_1 = \omega_1/2\pi$ is the frequency of the first-mode, j_c is the critical current density, and V_{grAl} is the sample volume, with values listed for each sample in the legend. Hilbert-shaped resonator samples are represented in blue, stripline samples in green, and Al-shunted stripline resonators in red. The error bars for the blue points show the standard deviation of the measured K_{11} for nominally identical resonators. In the legend, the samples are listed in decreasing K_{11} order, within each group. The blue up-oriented triangle corresponds to sample grAl#2 (highlighted in blue), and the green circle corresponds to grAl#1 (highlighted in green). The black line shows the calculated self-Kerr from Eq. (4), for a grain size $a = 4$ nm, which includes the 1 nm thickness of the aluminum oxide barrier. We estimate the main error source to be the photon number calibration, which can only be estimated within a factor of 10

Methods

Experimental apparatus. The dispersion relation for grAl resonators spans up to ~100 GHz. To cover this wide frequency range, we employ two complementary measurement setups, and we use the first mode as a link between them, via the cross-Kerr effect.

Low-frequency setup. The low-frequency part of the spectrum ($n = 1$–3), up to 20 GHz, is measured using microwave transmission and reflection measurements in a standard cQED setup[12] (Fig. 2b). The grAl stripline resonators (Fig. 2a) are mounted in a 3D waveguide (WG) sample holder, housed inside a hermetic copper shield coated with infrared-absorbing material. In this low-noise setup, all microwave lines are filtered above 8 GHz using commercial low-pass filters, circulators, and infrared absorbers identical to the setup in ref. [31] in order to reduce stray radiation. Even though the Hilbert-shaped grAl resonators and their aluminum sample holder (Fig. 2c) are designed to operate as kinetic inductance detectors (KIDs), which are required for the measurement of their high-frequency spectrum by means of direct optical spectroscopy (Fig. 2d), they were also measured by standard microwave transmission in the low-noise, shielded setup of Fig. 2b. The high level of filtering and superior shielding, offered by the measurement setup optimized for low frequencies, is required for the protection of the fundamental mode against stray excitations, which is essential for the measurement of its coherence and nonlinear properties (self-Kerr and cross-Kerr).

High-frequency setup. For the measurement of the effective plasma frequency, we use the wide-frequency band setup of Fig. 2d, consisting of an optical access cryostat coupled to a Martin–Puplett Interferometer (see Supplementary Discussion). The fundamental mode is continuously measured via microwave transmission measurements, while its frequency is shifted by cross-Kerr interactions with optically populated higher modes of the dispersion relation.

Data availability

All relevant data are available from the authors.

Received: 3 March 2018 Accepted: 31 August 2018
Published online: 24 September 2018

References

1. Anderson, P. Theory of dirty superconductors. *J. Phys. Chem. Solids* **11**, 26–30 (1959).
2. Beloborodov, I. S., Lopatin, A. V., Vinokur, V. M. & Efetov, K. B. Granular electronic systems. *Rev. Mod. Phys.* **79**, 469–518 (2007).
3. Cohen, R. W. & Abeles, B. Superconductivity in granular aluminum films. *Phys. Rev.* **168**, 444–450 (1968).
4. Deutscher, G., Fenichel, H., Gershenson, M., Grünbaum, E. & Ovadyahu, Z. Transition to zero dimensionality in granular aluminum superconducting films. *J. Low. Temp. Phys.* **10**, 231–243 (1973).
5. Parmenter, R. H. Isospin formulation of the theory of a granular superconductor. *Phys. Rev.* **154**, 353–368 (1967).
6. Dynes, R. C. & Garno, J. P. Metal-insulator transition in granular aluminum. *Phys. Rev. Lett.* **46**, 137–140 (1981).
7. Pracht, U. S. et al. Enhanced cooper pairing versus suppressed phase coherence shaping the superconducting dome in coupled aluminum nanograins. *Phys. Rev. B* **93**, 100503 (2016).
8. Abeles, B., Cohen, R. W. & Cullen, G. W. Enhancement of superconductivity in metal films. *Phys. Rev. Lett.* **17**, 632–634 (1966).
9. Deutscher, G. & Dodds, S. A. Critical-field anisotropy and fluctuation conductivity in granular aluminum films. *Phys. Rev. B* **16**, 3936–3942 (1977).
10. Chui, T., Lindenfeld, P., McLean, W. L. & Mui, K. Coupling and isolation: critical field and transition temperature of superconducting granular aluminum. *Phys. Rev. B* **24**, 6728–6731 (1981).
11. Rotzinger, H. et al. Aluminium-oxide wires for superconducting high kinetic inductance circuits. *Supercond. Sci. Technol.* **30**, 025002 (2017).
12. Wallraff, A. et al. Strong coupling of a single photon to a superconducting qubit using circuit quantum electrodynamics. *Nature* **431**, 162 (2004).
13. Gu, X., Kockum, A. F., Miranowicz, A., xi Liu, Y. & Nori, F. Microwave photonics with superconducting quantum circuits. *Phys. Rep.* **718–719**, 1–102 (2017).
14. Day, P. K., LeDuc, H. G., Mazin, B. A., Vayonakis, A. & Zmuidzinas, J. A broadband superconducting detector suitable for use in large arrays. *Nature* **425**, 817 (2003).
15. Emery, V. J. & Kivelson, S. A. Importance of phase fluctuations in superconductors with small superfluid density. *Nature* **374**, 434 (1995).
16. Deutscher, G., Gershenson, M., Grünbaum, E. & Imry, Y. Granular superconducting films. *J. Vac. Sci. Technol.* **10**, 697–701 (1973).
17. Pracht, U. S. et al. Optical signatures of the superconducting goldstone mode in granular aluminum: experiments and theory. *Phys. Rev. B* **96**, 094514 (2017).
18. Bachar, N. et al. Mott transition in granular aluminum. *Phys. Rev. B* **91**, 041123 (2015).
19. Bachar, N. et al. Signatures of unconventional superconductivity in granular aluminum. *J. Low. Temp. Phys.* **179**, 83–89 (2015).
20. Astafiev, O. V. et al. Coherent quantum phase slip. *Nature* **484**, 355 (2012).
21. Manucharyan, V., Koch, J., Glazman, L. & Devoret, M. Fluxonium: single cooper-pair circuit free of charge offsets. *Science* **326**, 113–116 (2009).
22. Gladchenko, S. et al. Superconducting nanocircuits for topologically protected qubits. *Nat. Phys.* **5**, 48 (2008).
23. Ho Eom, B., Day, P. K., LeDuc, H. G. & Zmuidzinas, J. A wideband, low-noise superconducting amplifier with high dynamic range. *Nat. Phys.* **8**, 623 (2012).
24. Puri, S., Boutin, S. & Blais, A. Engineering the quantum states of light in a kerr-nonlinear resonator by two-photon driving. *npj Quantum Inf.* **3**, 18 (2017).
25. Walls, D. F. & Milburn, G. J. *Quantum Optics*. (Springer-Verlag, Berlin Heidelberg, 2008).

26. Hutter, C., Tholén, E. A., Stannigel, K., Lidmar, J. & Haviland, D. B. Josephson junction transmission lines as tunable artificial crystals. *Phys. Rev. B* **83**, 014511 (2011).
27. Weissl, T. et al. Kerr coefficients of plasma resonances in josephson junction chains. *Phys. Rev. B* **92**, 104508 (2015).
28. Bourassa, J., Beaudoin, F., Gambetta, J. M. & Blais, A. Josephson-junction-embedded transmission-line resonators: From kerr medium to in-line transmon. *Phys. Rev. A.* **86**, 013814 (2012).
29. Masluk, N. A., Pop, I. M., Kamal, A., Minev, Z. K. & Devoret, M. H. Microwave characterization of josephson junction arrays: implementing a low loss superinductance. *Phys. Rev. Lett.* **109**, 137002 (2012).
30. Tancredi, G., Ithier, G. & Meeson, P. J. Bifurcation, mode coupling and noise in a nonlinear multimode superconducting microwave resonator. *Appl. Phys. Lett.* **103**, 063504 (2013).
31. Grünhaupt, L. et al. Loss mechanisms and quasiparticle dynamics in superconducting microwave resonators made of thin-film granular aluminum. *Phys. Rev. Lett.* **121**, 117001 (2018).
32. Bell, M. T., Sadovskyy, I. A., Ioffe, L. B., Kitaev, A. Y. & Gershenson, M. E. Quantum superinductor with tunable nonlinearity. *Phys. Rev. Lett.* **109**, 137003 (2012).
33. Hazard, T. M. et al. High kinetic inductance nbn nanowire superinductors. *arXiv:*1802.01723 (2018).
34. Niepce, D., Burnett, J. & Bylander, J. Nanowire superinductance fluxonium qubit. *arXiv:*1805.00938 (2018).
35. Baselmans, J. et al. A broadband superconducting detector suitable for use in large arrays. *J. Low. Temp. Phys.* **151**, 524–529 (2008).
36. Cardani, L. et al. New application of superconductors: high sensitivity cryogenic light detectors. *Nucl. Instrum. Methods Phys. Res. Sect. A: Accel., Spectrometers, Detect. Assoc. Equip.* **845**, 338–341 (2017). Proceedings of the Vienna Conference on Instrumentation 2016.
37. Sliwa, K. M. et al. Reconfigurable josephson circulator/directional amplifier. *Phys. Rev. X* **5**, 041020 (2015).
38. Lecocq, F. et al. Nonreciprocal microwave signal processing with a field-programmable josephson amplifier. *Phys. Rev. Appl.* **7**, 024028 (2017).
39. Koch, J. et al. Charge-insensitive qubit design derived from the cooper pair box. *Phys. Rev. A.* **76**, 042319 (2007).
40. Martin, D. & Puplett, E. Polarised interferometric spectrometry for the millimetre and submillimetre spectrum. *Infrared Phys.* **10**, 105–109 (1970).
41. Catalano, A. et al. Bi-layer kinetic inductance detectors for space observations between 80–120 ghz. *A&A* **580**, A15 (2015).

Acknowledgements

We are grateful to O. Buisson, D. Basko, G. Weiss, and A. Shnirman for fruitful discussions and to L. Radtke and A. Lukashenko for technical support. Facilities used waere supported by the KIT Nanostructure Service Laboratory (NSL). Funding was provided by the Alexander von Humboldt foundation in the framework of a Sofja Kovalevskaja award endowed by the German Federal Ministry of Education and Research. This work was partially supported by the Ministry of Education and Science of the Russian Federation in the framework of the Program to Increase Competitiveness of the NUST MISIS, contracts no. K2-2016-063 and K2-2017-081 (experiments), and K2-2-17-085 (theory).

Author contributions

N.M. and M.V.F. performed the theoretical study. L.G., F.V., and P.W. designed, fabricated the samples, and performed the measurements in the low-frequency setup. F.L.-B., O.D., M.C., and A.M. performed the MPI measurements and analysis. P.W., F.F., and W.W. designed and performed the switching current experiments. N.M. and I.M.P. lead the paper writing, while all other authors contributed to the text. IMP supervised and coordinated the project.

Additional information

Supplementary Information accompanies this paper at https://doi.org/10.1038/s41467-018-06386-9.

Competing interests: The authors declare no competing interests.

Reprints and permission information is available online at http://npg.nature.com/reprintsandpermissions/

Publisher's note: Springer Nature remains neutral with regard to jurisdictional claims in published maps and institutional affiliations.

Open Access This article is licensed under a Creative Commons Attribution 4.0 International License, which permits use, sharing, adaptation, distribution and reproduction in any medium or format, as long as you give appropriate credit to the original author(s) and the source, provide a link to the Creative Commons license, and indicate if changes were made. The images or other third party material in this article are included in the article's Creative Commons license, unless indicated otherwise in a credit line to the material. If material is not included in the article's Creative Commons license and your intended use is not permitted by statutory regulation or exceeds the permitted use, you will need to obtain permission directly from the copyright holder. To view a copy of this license, visit http://creativecommons.org/licenses/by/4.0/.

© The Author(s) 2018